International Journal of
Turbomachinery
Propulsion and Power

MDPI

Article

Influence of Radial Pressure Gradient on Secondary Flows: Numerical Study and Design Optimization for High-Speed Annular Sector Cascades†

Moritz Klappenberger [1,*], Christian Landfester [2], Robert Krewinkel [3] and Martin Böhle [1]

[1] Institute of Fluid Mechanics and Fluidmachinery, University of Kaiserslautern-Landau, 67663 Kaiserslautern, Germany
[2] Institute of Future Fuels, German Aerospace Center, 51147 Cologne, Germany
[3] Institute of Thermal Turbomachinery and Machine Dynamics, Graz University of Technology, 8010 Graz, Austria
* Correspondence: moritz.klappenberger@mv.rptu.de
† This manuscript is an extended version of our paper published in the Proceedings of the 16th European Turbomachinery Conference (ETC16)—Turbomachinery, Fluid Dynamics and Thermodynamics, Hannover, Germany, 24–28 March 2025; paper No. 321.

Abstract

Secondary flow phenomena have a significant influence on the generation of losses and the propagation of coolant on the turbine end walls. The majority of film cooling studies are carried out on linear rather than annular cascades due to the structural simplicity and ease of measurement integration of the former. This approach neglects the effects of the radial pressure gradient that is naturally imposed on the vortex flow in annular cascades. The first part of this paper numerically investigates the effect of the radial pressure gradient on the secondary flow under periodic flow conditions by comparing a linear and an annular case. It is shown that the radial pressure gradient has a significant influence on the propagation of the secondary flow induced vortices in the wake of the nozzle guide vanes (NGV). In the second part of the paper, a novel approach of a five-passage annular sector cascade is presented, which avoids the hub boundary layer separation, as is typical for this type of test rig. To increase the periodicity, a benchmark approach is introduced that includes multiple pointwise and integral flow quantities at different axial positions. Based on the optimized best-case design, general design guidelines are derived that allow a straightforward design process for annular sector cascades.

Keywords: annular sector cascade; secondary flow phenomena; radial pressure gradient; nozzle guide vane; numerical optimization

Academic Editor: Marcello Manna

Received: 22 April 2025
Revised: 7 July 2025
Accepted: 16 July 2025
Published: 5 August 2025

Citation: Klappenberger, M.; Landfester, C.; Krewinkel, R.; Böhle, M. Influence of Radial Pressure Gradient on Secondary Flows: Numerical Study and Design Optimization for High-Speed Annular Sector Cascades. *Int. J. Turbomach. Propuls. Power* **2025**, *10*, 18. https://doi.org/10.3390/ijtpp10030018

1. Introduction

Even though linear cascade testing offers a cost-effective and flexible approach for fundamental research (e.g., profile loss, wake mixing, trailing edge flows, etc.), it does not account for the effects of radial pressure gradients. These effects are evident in the formation and propagation of secondary flows, which not only cause losses but also significantly influence the heat load on the vane and endwall, as presented in early studies by Graziani et al. [1] and Blair [2].

To understand the emergence and development of secondary flow, Langston et al. [3] and Goldstein and Spores [4] provided crucial experimental findings. Wang et al. [5] subsequently devised a model of the observed vortex formations using smoke wire and laser

light visualization, demonstrating the emergence of the horseshoe and passage vortices. Figure 1 depicts a simplified model of the secondary flow within a turbine passage. As shown, the incoming boundary layer decelerates because it encounters an adverse static pressure gradient in front of the vane's leading edge. This induces a spanwise total pressure gradient within the boundary layer, driving the flow toward the end wall where it rolls up and splits into a pressure-side leg and a counter-rotating suction-side leg known as the horseshoe vortex. The weaker suction-side leg impinges on the suction side of the vane, while the pressure-side leg is drawn toward the suction side of the adjacent vane by the crosspassage pressure gradient. There is a consensus in the literature that the pressure-side leg forms a major part of the passage vortex, which is further intensified by the inlet boundary layer and the passage crossflow [3,5,6]. Once the passage vortex interacts with the counter-rotating suction-side leg, different models have been proposed. The model in Figure 1 aligns with Goldstein and Spores [4], suggesting that the suction-side leg separates from the endwall and continues as the so-called counter vortex. However, other authors, such as Sharma and Butler [7] and Sieverding and Van den Bosche [6], propose that it orbits around the passage vortex.

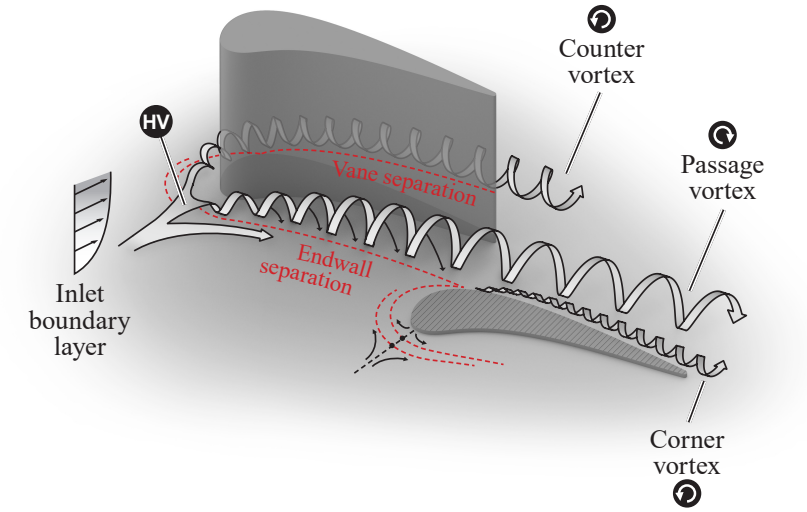

Figure 1. Simplified secondary flow vortex model (based on [8]).

The secondary flow field in an annular turbine guide vane is significantly affected by the radial pressure gradient that is inherent to swirling flows [9]. Studies with linear cascades therefore neglect the impact of this gradient on several key parameters, including the outlet flow angle, the spanwise distribution of losses, and the secondary flow phenomena [10]. Figure 2 illustrates the pressure field and the evolution of secondary flows in annular turbine cascades, which are influenced by two significant pressure gradients. The first is induced by the pressure difference between the suction and pressure side of neighboring vanes (turning flow). The second is induced by the curvature resulting from centrifugal acceleration (swirling flow). The radial pressure gradient arises from radial equilibrium and is given for axisymmetric and inviscid flows by Equation (1) [11].

$$\frac{\partial p}{\partial r} = \rho \cdot \frac{c_\phi^2}{r} \tag{1}$$

Although numerical studies facilitate the investigation of curved cascade designs, the resulting insights are limited by the absence of experimental validation.

The construction of an annular sector cascade faces two challenges: First, as with linear cascades, non-periodic flow conditions at the outer passages due to the finite number of vanes must be adressed. Second, outlet conditions need to be established to prevent

any (early) separation of the hub boundary layer due to the missing rotor [12]. The rotor typically eliminates the swirl generated by the guide vanes redirecting the flow back to the machine axis. A variety of solution approaches have been put forth in the existing literature, as discussed below. Nevertheless, there is currently no consensus on the optimal solution. To enhance periodicity, the most common approach is to utilize tailboards or boundary layer bleeds to regulate the mass flow through the border passages, thereby harmonizing the flow conditions [12]. To prevent hub boundary layer separation, Squire [13] employed a perforated plate to rebalance the radial pressure gradient. Povey et al. [14] utilized deswirling vanes to redirect the swirled flow back toward the machine axis. For a more comprehensive overview, Landfester [15] provides a detailed account. These approaches may potentially yield improvements in certain cases, but they were not deemed applicable to the study conducted here, as space limitations in the test room made it impossible to use deswirling vanes, and although the tailboard approach enhanced periodicity, hub boundary layer separation still occurred. The same issue was observed when attempting to energize the boundary layer through a high-momentum mass flux. Most cascades described in the literature share a common approach: The flow is guided within a cavity situated downstream of the passage and subsequently emitted toward the tank with a constant pressure. This study introduces a novel approach and provides clear design guidelines for annular cascades, eliminating the cavity and directing the flow toward the tank at its turning angle.

In the initial section of this paper, the impact of curvature on the secondary flow will be explored. Following this, the rationale behind the heightened complexity of experiments utilizing annular cascades in comparison to linear ones will be presented, along with an overview of the methodologies employed to overcome these challenges. Lastly, the novel approach will be presented. This manuscript corresponds to the paper published in the proceedings of the 16th European Turbomachinery Conference [16].

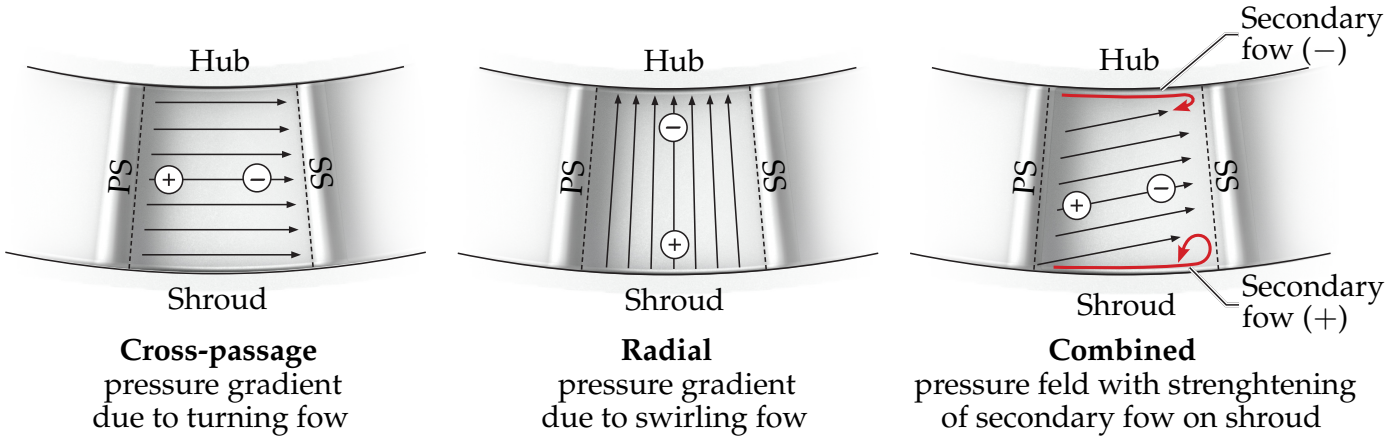

Figure 2. Pressure gradients in an annular cascade (adapted from Povey et al. [14]).

2. Numerical Setup and Mesh Independence Study

2.1. Periodic Case

Three-dimensional Computational Fluid Dynamics (CFD) simulations were conducted using the commercial software ANSYS, version 23.1. The steady-state simulations employed a compressible approach, and CFX was used as the solver. A linear (the linear geometry is referenced to the annular geometry at midspan) and an annular periodic-passage model were investigated, which are illustrated in Figure 3. As the secondary flows are more pronounced with a cylindrical profile (designed as a free vortex profile), rather than the aerodynamically optimized one the NACA used and defined as E^3, clear visual effects could be expected [17]. The profiles' geometric parameters can be found in

Table 1. For generating the block structured meshes, TurboGrid was used for both cases. In order to guarantee the presence of at least two cells in the viscous sublayer, the near-wall region of the vanes and endwalls was discretized with a $y^+ \approx 1$. A mass flow rate was defined as the inlet boundary condition. The outlet boundary condition was set to an average static pressure. A comprehensive overview of the boundary conditions can be found in Table 2. For turbulence modeling, the k-ω SST model by Menter [18] was used. The simulations were terminated once the RMS residuals dropped below 1×10^{-4} and the target values (velocity c, static pressure p_{stat}, and vane load F_{v}) exhibited convergence within a reasonable range (fluctuation around the mean value less than 1%, which was chosen as a practical threshold).

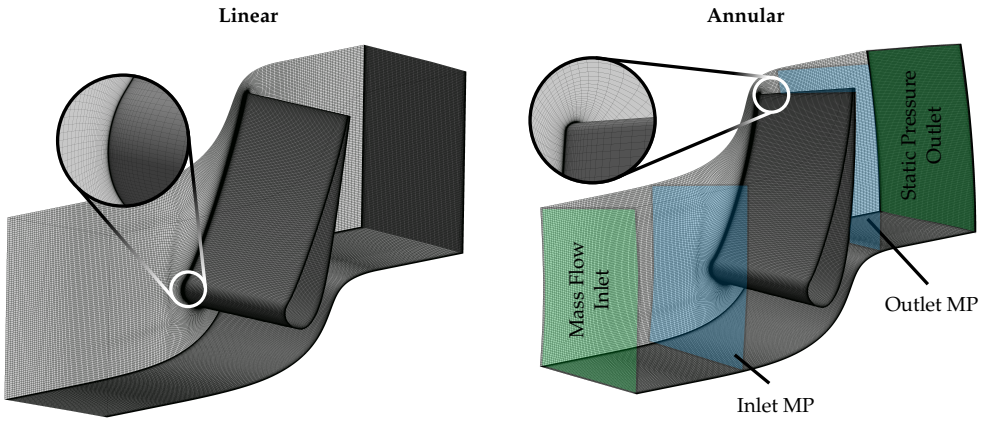

Figure 3. Linear and annular meshed fluid volume.

To guarantee mesh independence, the Grid Convergence Method based on the Richardson extrapolation [19] was employed. The mesh independence was investigated for four variables at different locations. Two monitor points were established within the fluid domain: one on each measurement plane (MP) and the load was calculated at the vane. To observe the inflow, the inlet MP was located at a distance of $2 \cdot c_{ax}$ upstream of the leading edge (LE), while the outlet MP was placed at a distance of $0.3 \cdot c_{ax}$ downstream of the trailing edge (TE) to monitor the outflow. The variables under consideration were the velocity, total pressure, Mach number, and vane load. To maintain concision, Table 3 and Figure 4 illustrate only the convergence example for the outflow velocity, because it is represenative for all other variables. Three meshes which were designated as coarse, medium, and fine were used. The mesh indenpendence study shows that the medium mesh met the requirements for the secondary flow analysis, as the error between the medium and the fine mesh was less than 0.1%. The grid convergence index amounted to 0.044%, and therefore, further grid refinement was not necessary.

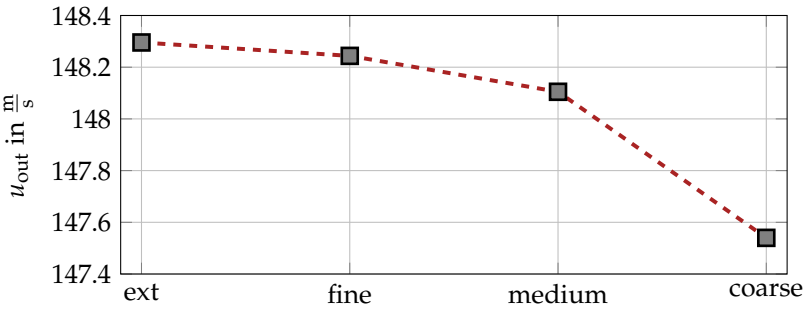

Figure 4. Grid convergence study showing u_{out} for different grid resolutions, with the estimated value 'ext' obtained from Richardson extrapolation.

Table 1. Vane and cascade parameters.

Parameter		Unit	Value
Chord length	c	mm	98.6
Axial chord	c_{ax}	mm	41.9
Inlet angle	β_{in}	°	90
Outlet angle	β_{out}	°	11.6
Blade span	h	mm	65.8
Blade pitch	S	mm	88.6
Blade pitch	S_{deg}	°	12
Aspect ratio	h/c	—	0.667
Radius hub	r_{hub}	mm	389
Radius mid	r_{mid}	mm	421.9
Radius shroud	r_{shroud}	mm	454.8
Number of vanes	N_{vane}	—	4
Number of passages	N_{pas}	—	5

Table 2. Boundary conditions: periodic case and cascade.

Region	Type	Value
Inlet Periodic	Mass Flow	0.4 $\frac{kg}{s}$
Inlet Cascade	Mass Flow	2.0 $\frac{kg}{s}$
Inlet	Temperature	298.15 K
Inlet	Turb. Intensity	5%
Outlet Periodic	Stat. Pressure	0.100165 MPa
Outlet Cascade	Stat. Pressure	0.100324 MPa
Hub, Shroud, Vane	Wall	no slip and adiabatic

Table 3. Mesh independence study for outlet velocity u_{out}.

Mesh	Elements	Deviation u_{out}	GCI	Time
Fine	14,477,034	0.094%	0.044%	7:52 h
Medium	6,092,801	0.382%	0.161%	2:55 h
Coarse	2,441,376	—	—	1:10 h

2.2. Cascade

To establish a robust optimization, the entire simulation process was set up in the Ansys Workbench, version 23.1. The mesh requirements for the cascades optimization are distinct from the periodic cases due to the necessity for a high number of geometry variations, and therefore, meshes with lower densities are required to reduce computational costs. For meshing the cascade, an unstructured mesh with tetraeders was used. Previous conducted investigations have demonstrated that an y^+ value exceeding 30 is sufficient for evaluating periodicity, since the focus is on the free flow field and not on near-wall interaction. Given the necessity of calculating numerous cases, the objective is to minimize calculation time, and therefore, the boundary layer resolution has been omitted. However, to prevent mesh-induced effects on the vortices, inflation layers were applied to ensure consistent cell sizes across all test cases. For turbulence modeling, the k-ω SST model was used. To ensure comparability, the pressure ratio was held constant at a value of 1.3 for all three cases, because the same operation point was used for both the single passage and the simulation of the experimental setup. The boundary conditions can be taken from Table 2, and the absolute values and geometric parameters from Table 1. Figure 5 illustrates the meshed simulation model of the annular sector cascade. The geometric parameters of the initial cascade are further explained in Section 4, where the

optimization process is introduced. The convergence criteria were identical to those in the periodic cases. The investigation of mesh independency was conducted in a manner analogous to that employed in the periodic case. The final mesh was the medium one that comprised 6,992,990 elements in total, which is approximately half the number of cells in the finest mesh.

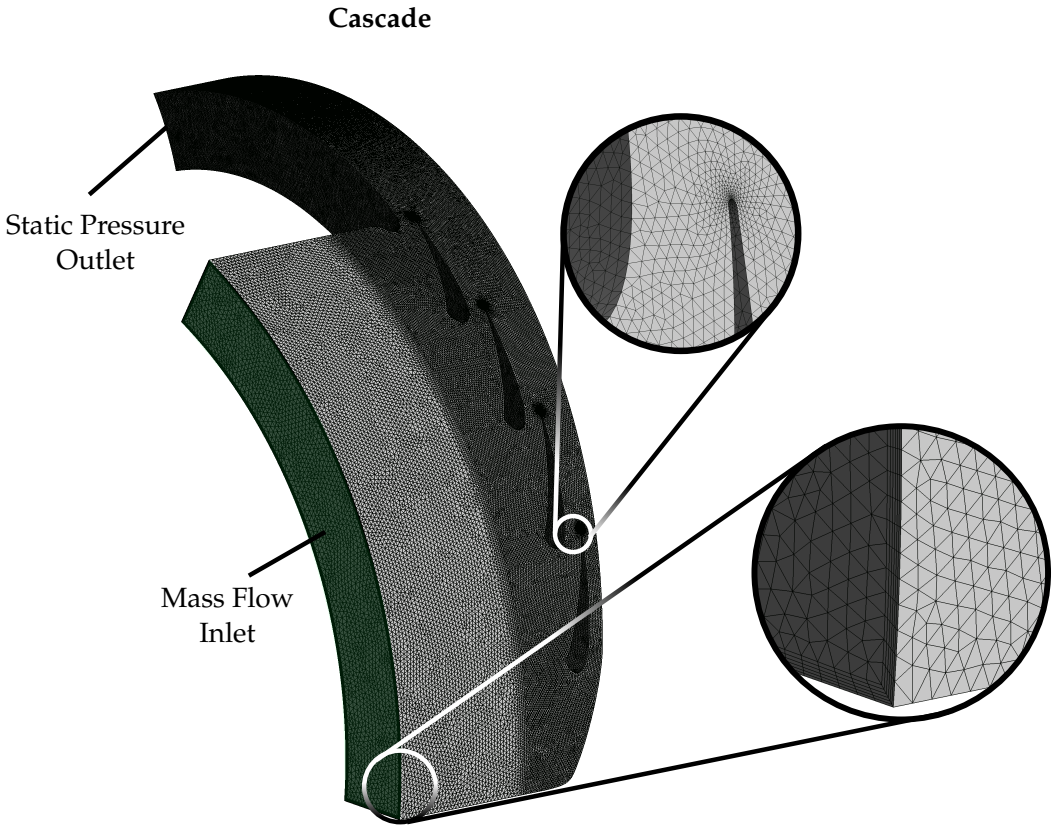

Figure 5. Meshed cascade fluid volume.

3. Secondary Flow Analysis

In order to investigate the secondary flow, an annular one-passage model (AP) with a curvature ratio of 0.25, similar to ratios used in modern gas turbines, was compared to a linear one-passage model (LP). As shown in Equation (2), the curvature ratio establishes a relationship between the chord length c and the hub radius r_{hub}.

$$c/r_{\text{hub}} = 0.25 \tag{2}$$

To visualize the aforementioned secondary flow structures, the Q-Criterion was employed in Figure 6a. It can be observed that the horseshoe vortex developed upstream of the vane's leading edge. In accordance with the explained topology in Section 1, pressure on the suction-side leg developed. The suction-side leg impinged on the front portion of the vane, whereas the pressure-side leg detached. The latter flowed across the passage and subsequently met the suction-side leg of the adjacent vane, which is shown in the detail. Figure 6a also illustrates the separation of the suction-side leg from the endwall caused by the interaction with the passage vortex, which, in contrast, stayed attached to the endwall. Given that the origin of the development of these structures was identical for the LP and AP, no differences were observed in the vicinity of the leading edge where the radial pressure gradient was not yet fully developed. However, the wake was significantly influenced by the radial pressure gradient, as illustrated in Figure 6b. At the outlet, the secondary-flow-induced vortices (SFIVs) of three vanes are visible labeled with the

numbers 1–3. It is evident that the SFIVs at the shroud reached further into the center of the stream than at the hub. Nevertheless, with increasing distance from the vane, hub boundary layer separation occurred (indicated by the red arrow), resulting in a shift of the SFIVs away from the hub toward the center of the passage. In order to facilitate the visualization of the differences between the AP and LP on the shroud side, the extension of the secondary-flow-induced vortices were marked in both cases with δ_{an} and δ_{lin}. This enabled the quantification of the vortices spreading from the shroud toward the midspan. The projection of δ_{an} in the LP made the difference clearly visible: By comparison, δ_{an} was two times larger than δ_{lin}. This resulted in a spreading of 20% toward the midspan in the AP case, which is solely attributable to the vortices situated at the shroud. Contrary to this, the spreading on the hub is of a lesser magnitude. As the streaming conditions were symmetric in the linear case, there was no discernible difference in the characteristics for the hub and shroud. Consequently, the spreading in the LP case was identical for the hub and shroud, accounting for 10% each.

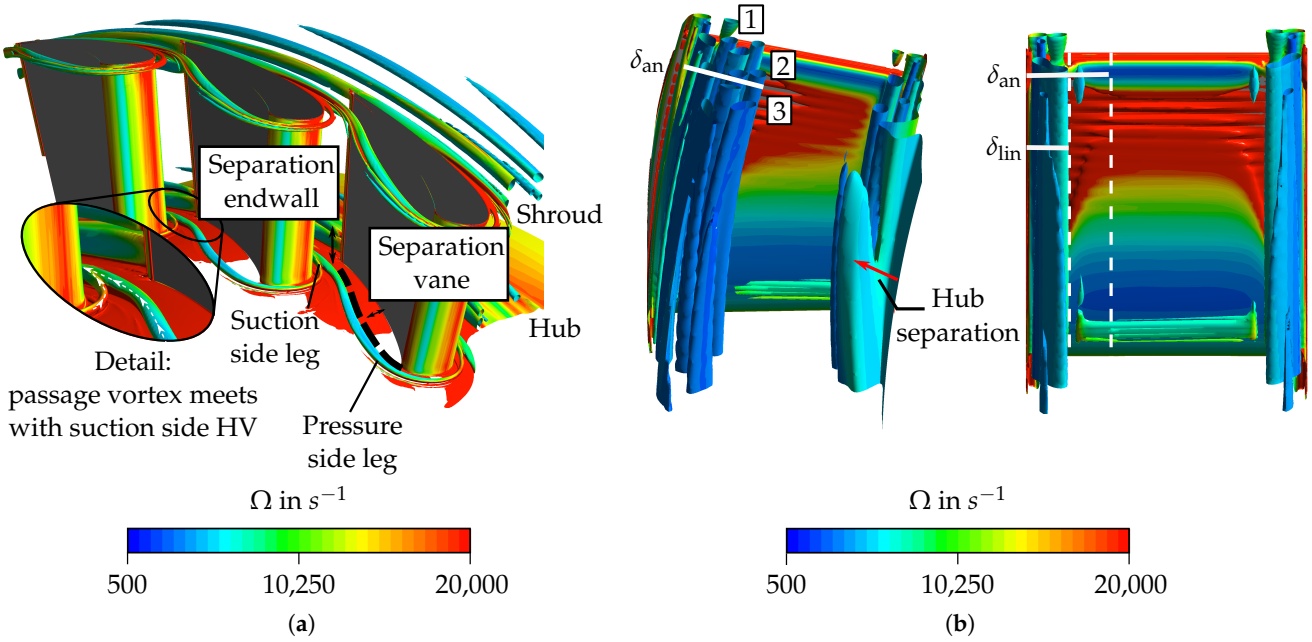

Figure 6. Visualization of secondary flow vorticity using the Q-criterion with (**a**) focus on the secondary flow development and (**b**) the secondary-flow-induced vortices in the wake.

To further evaluate the impact of curvature, the pressure coefficient (c_p), based on the outlet dynamic head, at three distinct spans ($0.1 \cdot h$, $0.5 \cdot h$, and $0.9 \cdot h$) was compared for both cases in Figure 7. No significant visual differences were evident upon comparing c_p along the spans of the linear case, which contributed to the symmetric flow. Near the leading edge, the pressure coefficient distribution remained nearly identical between both cases. However, further downstream—at approximately $0.4 \cdot c_{ax}$—the influence of the radial pressure gradient became evident. This resulted in a pressure decrease near the hub in the AP compared to the LP. With increasing span, the static pressure increased and was accompanied by the expected velocity reduction toward the shroud. Since the midspan curvature was identical in both cases, the pressure coefficient distributions exhibited no significant differences at that location.

Given the pronounced impact of the radial pressure gradient in the wake, the subsequent discussion is limited to the outlet measurement plane, situated at a distance of $0.3 \cdot c_{ax}$ downstream of the trailing edge. Figure 8 compares the Mach number, the entropy loss coefficient (ζ_s), and the secondary kinetic energy (SKE) distribution for the aforementioned

cases. In both cases, a notable decrease in Mach number was evident in the wake flow of the vanes, reaching a reduction of approximately 15%. As anticipated, the LP Mach number distribution was symmetrical due to the homogeneous circumferential pressure field. However, the influence of the radial pressure gradient was evident in the asymmetry of the distribution for the AP. Due to the higher curvature, the maximum Mach Number ($Ma \approx 0.49$) was located near the hub and decreased throughout the passage toward the shroud to $Ma \approx 0.43$, which represents a reduction of 12.2%. To visualize the influence of the above-mentioned propagation of the SFIVs at the shroud on the Mach number for both cases, a characteristic boundary of the influenced area has been marked. It can be observed that in the annular case, a gradual transition from secondary-flow-induced vortices to the actual wake region occurred throughout the entire passage. In contrast, in the linear case, the transition was confined to the region near the walls, with a constant wake flow present in the middle of the passage.

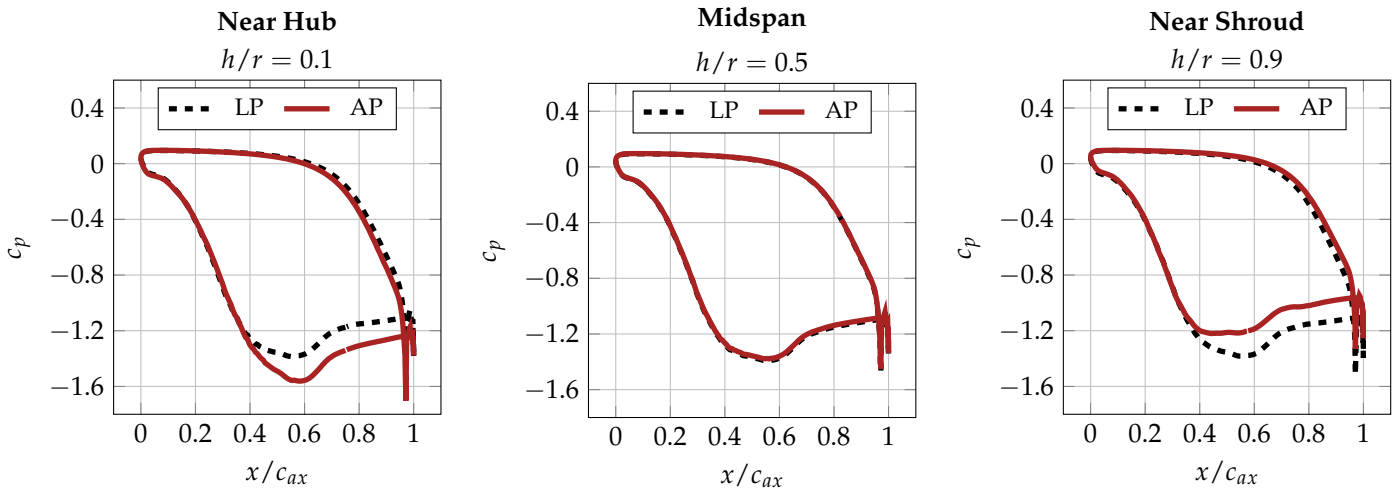

Figure 7. Pressure coefficient distribution based on the outlet dynamic head for the LP and AP along different spans downstream of the TE.

As secondary flow structures contribute to the overall loss of turbines, Figure 8 illustrates the entropy loss coefficient, following the definition by Denton [20], within the wake at the outlet MP. The distribution shows the characteristic patterns of turbine cascades, where the wake losses are dominant at the midspan, while near the endwalls, the secondary losses are the dominant feature. Considering the annular case, the results indicate that the losses at the hub were confined to the vortex region near the endwall, exhibiting a higher magnitude ($\zeta_s = 0.47$). In comparison, at the shroud, the losses extended further toward the passage center but with a lower magnitude peak ($\zeta_s = 0.33$). In the linear case, the loss distribution was symmetric, with identical maximum loss amplitudes at the hub and shroud ($\zeta_s = 0.41$). These values fall between those observed at the hub and the shroud in the AP case. When mass-flow-averaged losses at the outlet MP were considered, the total losses were the same for both cases, but with significant local differences. This leads to the preliminary conclusion that linear cascades are sufficient for evaluating a wider range of vanes, as the overall loss development is the same. However, for optimizing the vane itself, the annular cascade provides the benefit of more realistic loss patterns, making it more relevant for engine applications.

An adequate method to quantify the extent of secondary flow is to consider the secondary kinetic energy (SKE). Following the definition by Moore and Adhye [21], a main flow direction tangential to the trailing edge is defined. The velocity components orthogonal to this direction represent the secondary flow. For the linear case, the inertial

coordinate system is rotated (rotation angle β_{out}) to align with the main flow direction, whereas for the annular case, a rotated cylindrical coordinate system is more appropriate. The secondary kinetic energy (SKE) is defined as follows for both the LP and AP cases, as given in Equation (3), where the secondary velocity components are normalized by the reference velocity (main flow).

$$SKE = \frac{\hat{u}^2 + \hat{w}^2}{\hat{v}^2_{\text{ref}}} = \frac{\hat{u}^2_{\text{rad}} + \hat{w}^2_{\text{cyl}}}{\hat{u}_{\text{circ,ref}}} \tag{3}$$

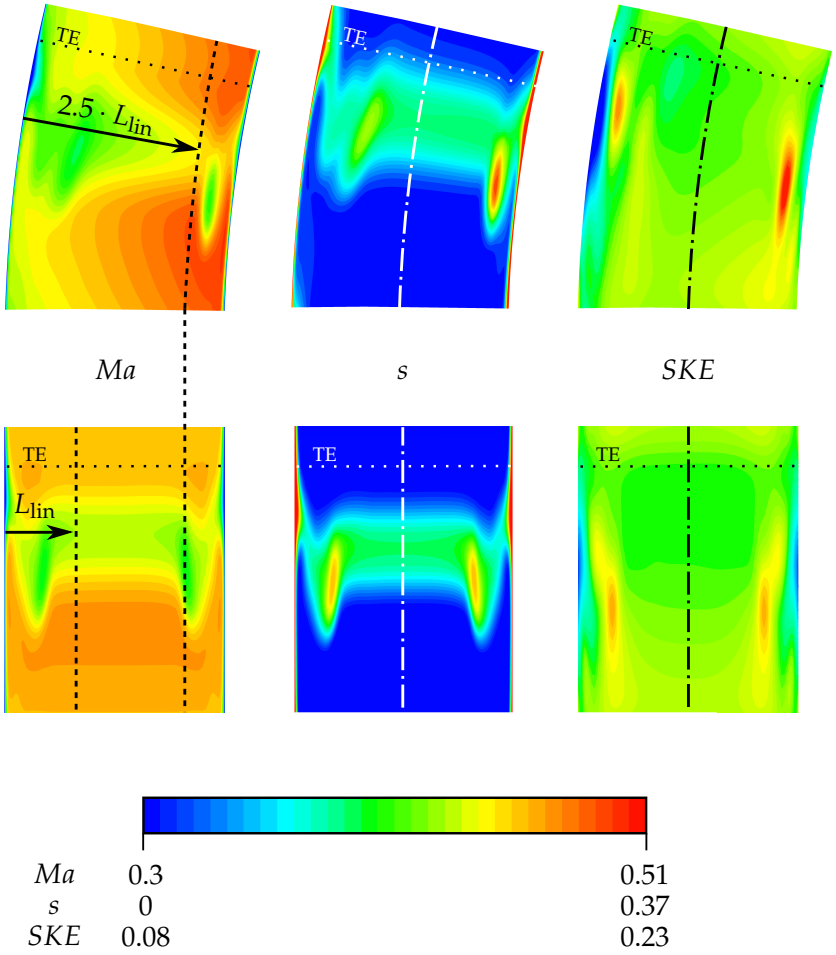

Figure 8. Comparison of the Mach number, entropy loss coefficient, and secondary kinetic energy distribution at the outlet MP, located $0.3 \cdot c_{ax}$ downstream of the TE, for the AP and LP.

The distribution of secondary kinetic energy, shown in Figure 8, supports the aforementioned conclusions. In the linear case, the SKE distribution was nearly symmetrical, with the highest energy levels appearing equally in the SFIVs at both the hub and shroud ($SKE = 0.21$). Based on the amount of secondary kinetic energy near the midspan, it can be seen that the wake flow deviated from the trailing edge angle of the vane. This indicates that the flow was overturned relative to the metal angle of the vane. In the annular case (AP), the maximum SKE was found within the SFIV near the hub ($SKE = 0.24$). Toward the midspan, the energy decreased and reached levels comparable to those in the linear case. On the shroud side, the SKE was lower, amounting to $SKE = 0.21$. Notably, the vortex core near the endwall was followed by a small region of lower energy, which was succeeded by a secondary increase. This indicates that vortices near the shroud appear to have been separated, and the passage vortex remained attached to the endwall, while the separated suction-side leg of the horseshoe vortex was displaced further toward the

midspan. In contrast, on the hub side, no such distinction was observed, as the pressure gradient forced all vortices toward the endwall.

The influence of the radial pressure gradient is evident in all three contour plots. The SFIV on the shroud side expanded significantly further toward the midspan, while its counterpart was spatially limited to the hub. It can be concluded that the secondary flow structures were reinforced on the shroud by the radial pressure gradient, whereas they were weakened on the hub.

4. Cascade Optimization

The analysis of the periodic case demonstrated a notable impact of the radial pressure gradient on the propagation of the secondary flow, indicating the necessity for a more detailed examination of the influence of the curvature ratio. In future parametric studies, different curvature ratios should be performed. Therefore, it is essential to validate the CFD setup, and experimental studies are necessary. To address the above-mentioned challenges of boundary layer separation and flow periodicity, the methods sugessted in [12–14] have been unable to produce satisfactory results, as already discussed in Section 1. Most previously described designs of annular cascades have as a common feature that, downstream of the vane, the air enters a cavity (compare Figure 9a), or deswirling vanes are used.

It has been established in previous studies [15] that a numerical optimization of the cascade—focusing solely on flow periodicity—is crucial due to the limited number of passages in a sector cascade. First, an approach was adopted that had previously been developed for an axisymmetrically contoured profile on the high-speed turbine test rig of the institute [22]. Figure 9a illustrates the parameterized fluid volume of the cascade. To enhance periodicity, a tailboard was used to regulate the mass flow through the lower passage and a backward-facing step to control it in the upper passage. The limiting wall represents the pressure on the suction side of the missing neighboring vanes. The initial simulation configuration comprises five discrete parameters: the tailboard angle, tailboard length, facing step length, outlet extension, and outlet angle. Although it was feasible to increase the periodicity of the flow by modifying the tailboard parameters, the hub boundary layer separation commenced in all configurations at a distance less than $0.3 \cdot c_{ax}$ downstream of the TE, which is the location of the outlet measurement plane. Consequently, the flow was strongly influenced, and it would not have been feasible to make any reliable assessments of the influence on secondary flow structures. In addition to the approach presented here, attempts have been made to prevent separation using deswirling vanes, as suggested by Povey et al. [14] and by boundary layer control [13]. Neither of these options prevented the boundary layer separation and therefore will not be discussed further.

To understand the idea of the approach introduced in the following section, it is essential to explain the origin of the boundary layer separation. Figure 10a therefore provides a visual representation of the wall shear stress, with streamlines on the hub, while Figure 10b illustrates the complete fluid flow through the cascade. It can be observed that a recirculation area (RA), indicated by the black arrow, was formed within the cavity situated directly behind the vanes. The subsequent evolution of this phenomenon can be explained as follows: The higher curvature of the hub results in a higher velocity than that near the shroud, leading to an increase in static pressure from the hub to the shroud (compare Section 1). The presence of the cavity behind the vanes allows the flow to deviate from the intended flow path in the axial direction. This results in the compensation of the radial pressure gradient by mass transfer from the shroud to the hub, leading to the formation of the observed RA. It is evident that the flow detached due to the adverse pressure gradient at the point of convergence between the RA and the passage outflow. The simulations

demonstrated that the size of the RA was proportional to the outlet extension. As the cavity lengthened, the RA increased in size. It was observed that the separation line exhibited a slight downstream shift with larger RAs, as the momentum decreased due to friction. However, the separation influence remained significant. In alignment with the findings of Landfester [15], a reduction in outlet extension resulted in an earlier detachment of the hub boundary layer.

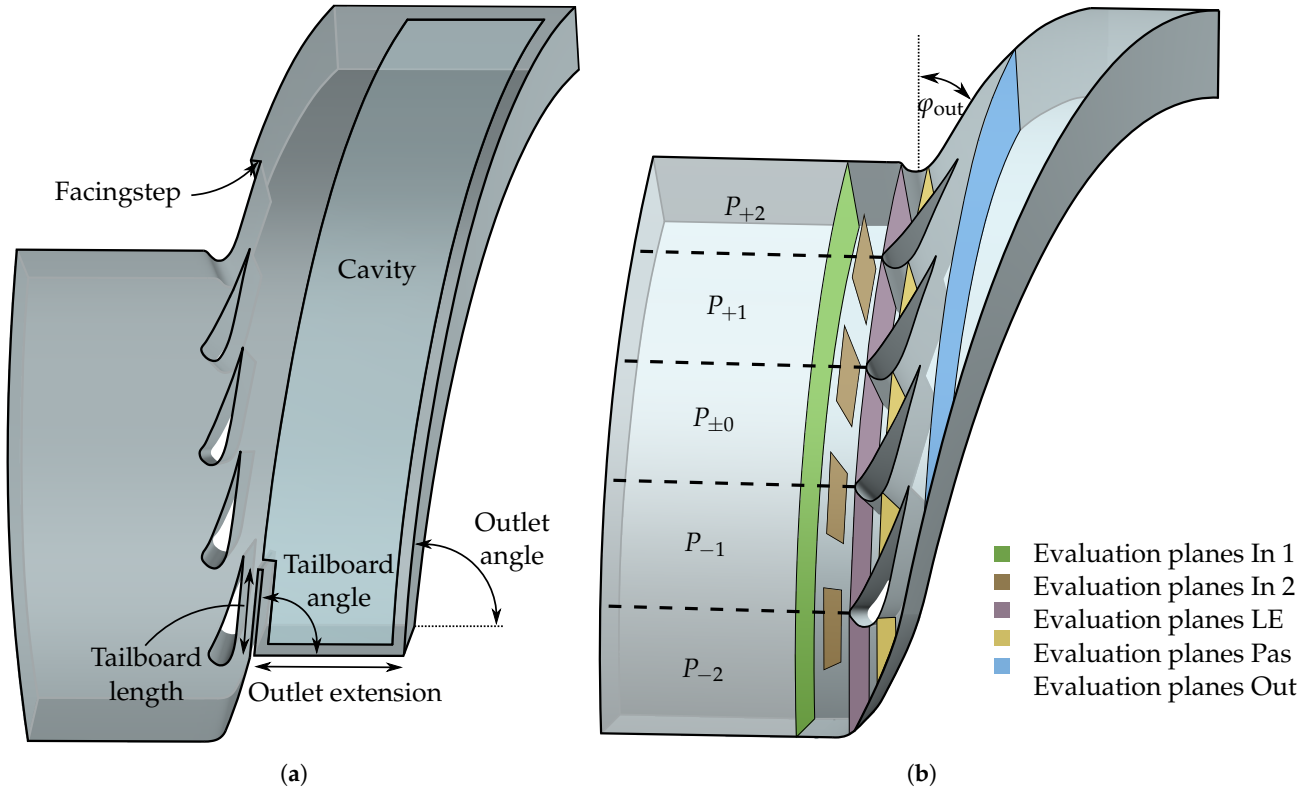

Figure 9. Visualization of the cascades fluid volume: (**a**) initial parametrized approach and (**b**) final approach with planes for *BM* evaluation and defintion of φ_{out}.

The new approach is based on the idea of completely eliminating the recirculation. Consequently, the cavity was eliminated. The limiting walls extend from the approximated pressure on the suction side of the lower and upper passage wall. This results in a more curved outflow than in the former presented approach with a cavity, because the outflow angle remains constant. With the cavity situated downstream of the vanes, the flow widens, and therefore, its discharge angle is significantly lowered. Figure 9b presents the new approach. By employing this design, it was possible to prevent the hub boundary layer separation, as shown below.

The subsequent optimization results are mainly discussed using the Mach number, as this is a good indicator of periodicity. Figure 11 compares the aforementioned approaches using the Mach number distribution and streamlines at the outlet MP. When using the cavity, the value of the Mach number in the vicinity of the hub was markedly lower than that observed in the remainder of the passage, which is indicative of the phenomenon of hub boundary layer separation. The separation become evident when the flow path is visualized with streamlines. The separation set in downstream of passage P_{-2} and propagated over the remaining passages toward the outlet. The wake was therefore significantly influenced, and it would not be possible to reproduce the wake flow of the aforementioned annular periodic case. In contrast, the boundary layer separation did not appear with the new approach. This can be seen from the homogeneous Mach number distribution over the

entire span of all five passages. Additionally, each streamline followed its defined circular path, indicating a stationary and equilibrium state.

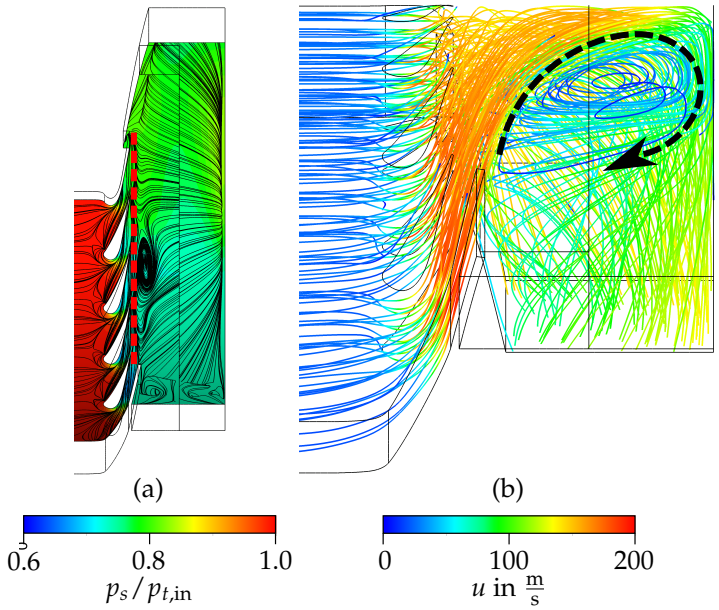

Figure 10. Development of the recirculation area: (**a**) surface streamlines on the hub and (**b**) recirculation area inside the cavity.

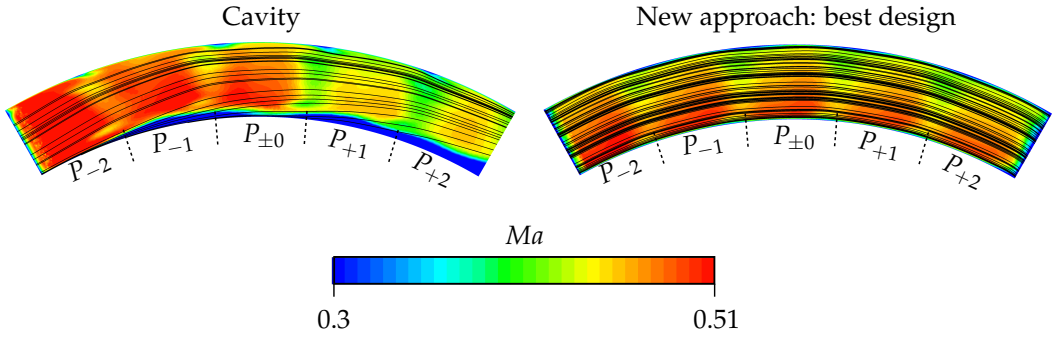

Figure 11. Comparison of the different approaches and visualization of the hub boundary layer separation.

Having solved the problem of the boundary layer separation, the optimization process focused consequently on establishing periodicity. Therefore, the outlet angle (compare Figure 9b) remained the only parameter, which was varied in a range from 73° to 83°. In order to quantify the quality of the flow periodicity, which is a necessary step in optimization processes, a benchmark formulation has to be established, which is referred to as *BM*. The benchmark was defined with accordance to the approach introduced by Landfester [15] as follows:

$$BM = \frac{1}{j}\sum_{j}(BM_{Ma_j} + BM_{\dot{m}_j} + BM_{\beta_j}) + BM_{\text{load}} \cdot \left(\frac{\Pi_{\text{target}}}{\Pi_{\text{real}}}\right)^4 \tag{4}$$

It consists of four independent sub-*BM*s, each pertaining to a specific variable: Mach number (Ma), flow angle (β), mass flow ($\dot{m}$), and the resulting force (F) on the vanes. The benchmark ensures that all parameters are evaluated concurrently so that the final configuration accounts for all criteria simultaneously. In instances where unfavorable parameter setups resulted in Mach numbers exceeding the speed of sound, the outlet pressure was increased in an iterative manner to bring the Mach number below 1, as compression shocks worsen the convergence of the simulation. To account for the fact that

the target pressure ratio would not be achieved in these cases, a correction was made using the penalty term $\frac{\Pi_{\text{target}}}{\Pi_{\text{real}}}$. As illustrated in Figure 9b, the cascade can be divided into five independent passages. For each passage, different measurement planes are defined where the average of the flow variables is determined. Table 4 enumerates the planes utilized for the sub-benchmark (BM_{sub}) calculation. The BM_{sub} values signify the relative deviation of the passages in relation to the mid passage ($P_{\pm 0}$) and are defined as stated in Equation (5). The index j depends on the number of evaluation planes used for each variable. As only four vanes were present for the vane load, the mean value of the second and third vane was calculated and used for calculating the deviation for all vanes.

$$BM_{\text{sub}_j} = \sum_{i=-2}^{2} \frac{|X_i - X_{P_{\pm 0}}|}{X_{P_{\pm 0}}}; \quad BM_{\text{load}} = \sum_{i=1}^{4} \frac{|F_{\text{load}_i} - \overline{F_{\text{load2,3}}}|}{\overline{F_{\text{load2,3}}}} \tag{5}$$

Given that the optimization was initially configured to examine five parameters, a multitude of potential combinations could have been explored. Accordingly, a design of experiment (DoE) was devised at the outset. In light of the findings of a preliminary study, it was possible to limit the scope to a single parameter. This allowed for the implementation of a full factorial and eliminating the potential for confounding variables.

Table 4. Benchmark evaluation type and location.

Sub-BM	Type	Location
Ma	mass-flow and area average *	In 1, LE, Pas, Out
$\dot{m}$	mass flow average	LE
F	absolute	Vanes
β	average	In 2

* mass-flow average for p_t, area average for p_s [23].

Figure 12 illustrates that the introduced benchmark definition allowed for the identification of a clear minimum. Two stages of optimization were carried out. The first examined a wide range of angles to estimate the region of best periodicity. The second stage examined the region around the minimum to find the best angle. The data were fitted using a third-degree polynomial, resulting in the following expressions:

Stage 1:

$$BM(\varphi) = 2.99\text{e}^{-2} \cdot \varphi^3 - 6.832\text{e}^{0} \cdot \varphi^2 + 5.197\text{e}^{2} \cdot \varphi - 1.316\text{e}^{4} \tag{6}$$

Stage 2:

$$BM(\varphi) = -4.492\text{e}^{-1} \cdot \varphi^3 + 1.221\text{e}^{1} \cdot \varphi^1 - 1.089\text{e}^{3} \cdot \varphi + 3.195\text{e}^{5} \tag{7}$$

The sensitivity analysis was conducted in two stages. In the initial phase of the investigation, the angles in question were examined within a range of 73° to 83°, with a step size of 1°. In the second stage of the sensitivity study, angles between 78.5° and 79.5° were investigated with a step width of 0.1°. In both stages, the minimum value of the *BM* was observed at an angle of 79°. To validate that at this angle the requirements of periodicity were met, an additional comparison was made between the Mach Number distribution of two angles—one smaller and one larger than the optimal design (78° & 80°). (The initial stage was selected, as the deviations were more pronounced. The characteristics of the second stage were analogous to those of the initial stage, though to a lesser extent.) The contour plots of the Mach number can be located at the previously introduced outlet measurement plane and are presented in Figure 13. To facilitate a more detailed comparison, the diagrams in Figure 14 illustrate the impact of angle deviation. The Mach number is plotted along the midspan at the outlet MP. It is evident that the periodicity was markedly

higher at the *BM* minima. At the outer passages, P_{-2} and P_{+2}, a velocity increase and decrease, respectively, can be identified for the different angles of 78° and 80°. Furthermore, it can be observed that with smaller angles, greater acceleration of the flow in the lower passage took place due to the reduction in outlet cross-section. The opposite occurred at the upper passage, resulting in a lower velocity. With higher angles, the change in the cross-section reversed, leading to the opposite velocity effects. Despite the significant increase in periodicity, the diagrams still demonstrate differences in the wake behavior of the border passages, indicating that the influence of the missing vanes cannot be fully eliminated. However, the periodicity of the three middle passages was sufficient to assume periodic conditions when an angle of 79° was used. A comparison of the *Ma* distributions of five periodic passages with those of the optimized cascade visualized in Figure 13 reveals a high degree of agreement in both the observed structures and the absolute values. As the mesh of the periodic case was structured and significantly finer than that of the cascade, the wake region was more detailed, and the borders of the vortices were more accurate. However, the simplifications made to reduce computing time were sufficient and produced satisfactory results of the optimization.

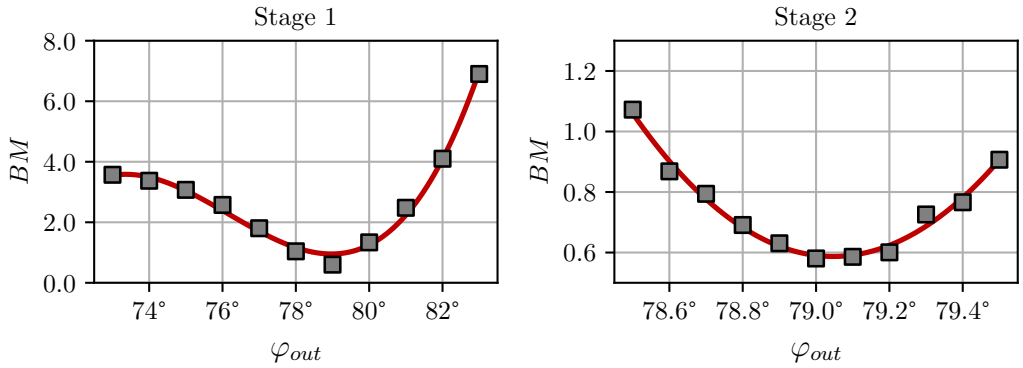

Figure 12. Benchmark results for varying outlet angles.

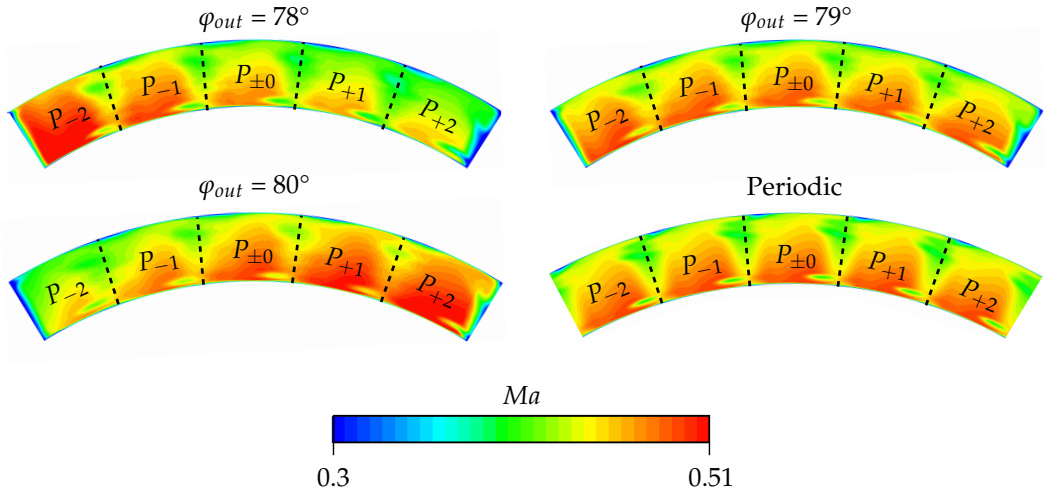

Figure 13. Visualization of the *Ma* distribution at different outlet angles of the cascade and the AP results as reference.

As a concluding comparison, Figure 15 presents the mass-averaged Mach number and pitch angle for five distinct outlet angles (75°, 77°, 79°, 81°, and 83°). The previously discussed trends, as well as the optimal outlet angle of 79°, are confirmed in this figure. It can be observed that a decrease in the outlet angle led to a 25% increase in Mach number in passage P_{-2} and a 9.5% decrease in passage P_{+2} compared to the middle passage. This behavior is associated with a cross-sectional narrowing in the first passage and a

corresponding widening in the last passage. As the outlet angle approached the optimal value of 79°, these deviations diminished, resulting in an almost periodic distribution. Conversely, for angles greater than 79°, the narrowing and widening effects reversed, leading to a decrease in Mach number in the first passage and an increase in the last passage. Notably, deviations for excessively large outlet angles were more pronounced than for excessively small ones. The Mach number deviation for P_{-2} at an outlet angle of 83° was 48% compared to the optimal middle passage $P_{\pm 0}$ at 79°. This effect was also reflected in the steeper performance degradation of Stage 1 for outlet angles exceeding 79°.

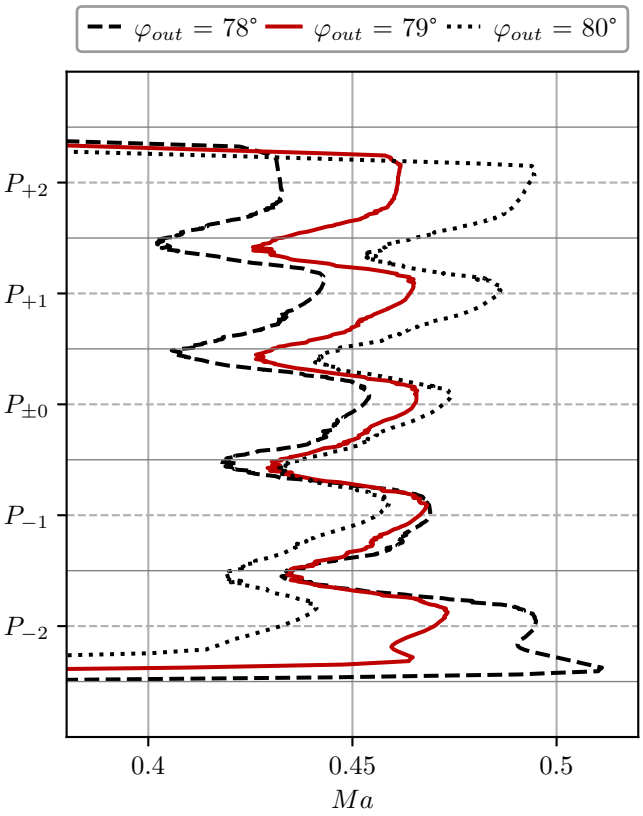

Figure 14. Visualization of the periodicity differences between the outlet angles of 78°, 79°, and 80°.

A similar trend was observed for the pitch angle. At smaller outlet angles, the flow was underturned, while at larger angles, it became overturned. This effect diminished with increasing passage number, leading to smaller deviations in the last passages compared to the first. When comparing the periodicity of Mach number and pitch angle, it is evident that the Mach number distribution remained highly periodic across all passages, except for P_{-2}, which was slightly elevated compared to the others. While the pitch angle also exhibited satisfactory periodicity in the optimal case, its deviations between passages were slightly larger than those of the Mach number. Overall, the results demonstrate that the pitch angle is more significantly influenced than the Mach number. The periodicity was satisfactory and acceptable for the middle passages, though downstream of vanes 1 and 4, the pitch angle distribution lacked periodicity. Nevertheless, the angles downstream of vanes 2 and 3 remained nearly identical. To derive a good starting point for an optimization, it is suitable to compare the best outlet angle of the cascade to the turning angle (78.4°) of the profile. The results indicate that, for the initial simulation, a slight variation around the profile's metal angle serves as a good starting point for further optimization.

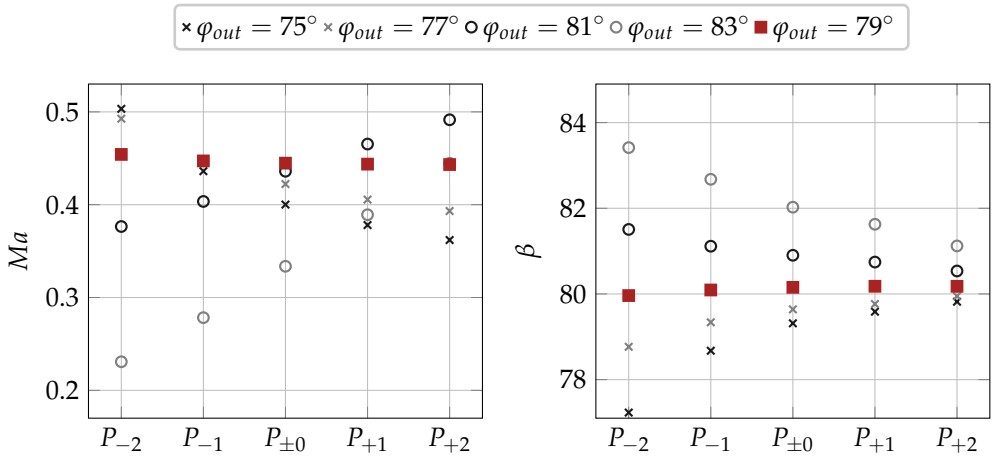

Figure 15. Mass-averaged Mach number and pitch angle for different outlet flow angles at each passage at outlet MP.

5. Conclusions

This study provides a comprehensive overview of the influence of the radial pressure gradient on secondary flow structures, with a comparison of a linear and annular periodic one-passage turbine model. Since the influence of the radial pressure gradient can probably be better analyzed, a cylindrical NACA E^3 profile with a pronounced secondary flow (instead of an aerodynamically optimized profile) was used [17]. The aim was to quantify the necessity of conducting studies with annular cascades in addition to linear ones, as the latter fail to account for the impact of the radial pressure gradient. While numerical studies provide valuable insights, experimental validation remains important; therefore, a novel approach for designing annular sector cascades for test rigs was provided. This new approach avoids the two main difficulties encountered in designing annular cascades and allows experiments to be carried out with machine-like Mach and Reynolds numbers. The main conclusions of the present study are as follows:

- The influence of the radial pressure gradient is significant for the present blade solidity and loading conditions and should be considered in the design of axial turbines. Whereas in the linear case the secondary flow structures develop symmetrically, in the annular case, the wake flow of the NGV in particular is influenced by the curvature. This leads to a reinforcement of the secondary flow at the shroud and a weakening at the hub.
- In order to investigate the influence of curvature with test rigs, annular cascades have to be designed. Due to the lack of rotor blades, hub boundary layer separation is a problem, which must be addressed. Consequently, an optimization process involving CFD is an essential component of the design process.
- It has been demonstrated that the conventional methodologies described in the literature result in the formation of a recirculation zone, which leads to the undesired separation. By eliminating the cavity and aligning the outlet with the natural fluid flow, the separation was completely eliminated.
- The presented design and optimization process is well suited for testing a specific vane geometry, as the outlet angle φ_{out} depends on the vane itself. In addition to aerodynamic advantages, this cascade design reduces the axial length of the test section compared to the geometries in the literature, making it beneficial in space-constrained environments. However, the cavity approach offers greater flexibility for testing different vane geometries and is more cost-effective in manufacturing, as it does not require freeform components.

- In order to ensure periodicity, a benchmark approach was employed, which made it possible to quantify the periodicity mathematically and thus to optimize it. By varying the cascades outlet angle, a distinct minimum and, therefore, an optimal design could be found. The following analysis demonstrated that the prediction of the optimum was correct and provided the highest periodicity.

While the preceding study presented only numerical results, the cascade design should be validated with experimental data in the next study. Furthermore, heat transfer measurements will be carried out to investigate the influence of curvature on film cooling performance when ejecting out of an upstream situated slot like the purge slot.

Author Contributions: Conceptualization, C.L. and M.B.; methodology, M.K. and C.L.; software, M.K.; validation, M.K., R.K., and C.L.; formal analysis, M.K. and C.L.; investigation, M.K.; resources, M.B.; data curation, M.K.; writing—original draft preparation, M.K.; writing—review and editing, M.K., C.L. and R.K.; visualization, M.K. and C.L.; supervision, M.B.; project administration, M.B.; funding acquisition, M.B. All authors have read and agreed to the published version of the manuscript.

Funding: The results presented in this paper were obtained within the framework of the DFG-funded project "Influence and Sensitivity of Turbine Cascade Curvature on Film Cooling Effectiveness" (DFG, German Research Foundation). Grant number: 520309913. The publication costs were covered by Euroturbo.

Institutional Review Board Statement: Not applicable.

Informed Consent Statement: Not applicable.

Data Availability Statement: The data are fully available for sharing upon direct request to the main author of this paper.

Acknowledgments: During the preparation of this manuscript, the authors used DeepL 2025 and ChatGPT-4o for grammar and spelling corrections. The authors have reviewed and edited the output and take full responsibility for the content of this publication.

Conflicts of Interest: Author Christian Landfester was employed by the company German Aerospace Center. The remaining authors declare that the research was conducted in the absence of any commercial or financial relationships that could be construed as a potential conflict of interest.

Nomenclature

Latin

p	pressure
c	chord length
h	blade span
S	blade pitch
r	radius
N	count
A	area
u	velocity
F	load
BM	benchmark
$\dot{m}$	mass flow
Ma	Mach number
s	entropy
SKE	secondary kinetic energy
c_p	$\frac{p_t - \overline{p_{t,\text{out}}}}{\overline{p_{\text{dyn}}}}$ dimensionless loss coefficient
T	temperature
H	enthalpy

Abbreviations

NGV	nozzle guide vane
HV	horseshoe vortex
SS	suction side
PS	pressure side
CFD	computational fluid dynamics
RMS	root mean square
GCI	grid convergence index
AP	annular one-passage model
LP	linear one-passage model
SFIV	secondary-flow-induced vortex
TE	trailing edge
RA	recirculation area
MP	meassurement plane
DoE	design of experiment

Greek

β	pitch angle
φ	outlet angle cascade
Ω	vorticity
ζ_s	$\frac{T_{out}\Delta s}{H_t - H}$ entropy loss coefficient
Π	pressure ratio
δ	extension of SFIV

Superscripts

$\widehat{\ }$	dimensionless quantity
pas	passage
v	vane
ax	axial
in	inlet
out	outlet
deg	degree
an	annular
lin	linear
s	static
t	total
cyl	cylindrical
rad	radial
circ	circumferential
ref	reference

References

1. Graziani, R.A.; Blair, M.F.; Taylor, J.R.; Mayle, R.E. An Experimental Study of Endwall and Airfoil Surface Heat Transfer in a Large Scale Turbine Blade Cascade. *J. Eng. Power* **1980**, *102* , 257–267. [CrossRef]
2. Blair, M.F. An Experimental Study of Heat Transfer and Film Cooling on Large-Scale Turbine Endwalls. *J. Heat Transf.* **1974**, *96*, 524–529. [CrossRef]
3. Langston, L.S.; Nice, M.L.; Hooper, R.M. A Three-Dimensional Flow Within a Turbine Cascade Passage. *J. Eng. Power* **1977**, *99*, 21–28. [CrossRef]
4. Goldstein, R.J.; Spores, R.A. Turbulent Transport on the Endwall in the Region Between Adjacent Turbine Blades. *J. Heat Transf.* **1988**, *110*, 862–869. [CrossRef]

5. Wang, H.P.; Olson, S.J.; Goldstein, R.J.; Eckert, E.R.G. Flow Visualization in a Linear Turbine Cascade of High Performance Turbine Blades. *J. Turbomach.* **1997**, *119*, 1–8. [CrossRef]
6. Sieverding, C.H.; Van den Bosche, P. The use of coloured smoke to visualize secondary flows in a turbine-blade cascade. *J. Fluid Mech.* **1983**, *134*, 85–89. [CrossRef]
7. Sharma, O.P.; Butler, T.L. Predictions of Endwall Losses and Secondary Flows in Axial Flow Turbine Cascades. *J. Turbomach.* **1987**, *109*, 229–236. [CrossRef]
8. Takeishi, K.; Matsuura, M.; Aoki, S.; Sato, T. An Experimental Study of Heat Transfer and Film Cooling on Low Aspect Ratio Turbine Nozzles. *J. Turbomach.* **1990**, *112*, 488–496. [CrossRef]
9. Sieverding, C.H.; van Hove, W.; Boletis, E. Experimental Study of the Three-Dimensional Flow Field in an Annular Turbine Nozzle Guide Vane. *J. Eng. Gas Turbines Power* **1984**, *106*, 437–444. [CrossRef]
10. El-Batsh, H.M. Effect of the Radial Pressure Gradient on the Secondary Flow Generated in an Annular Turbine Cascade. *Int. J. Rotating Mach.* **2012**, *2012*, 509209. [CrossRef]
11. Lakshminarayana, B. *Fluid Dynamics and Heat Transfer of Turbomachinery*; Wiley: New Delhi, India, 1996; ISBN: 978-0-471-85546-0.
12. Hirsch, C. *Advanced Methods for Cascade Testing*; North Atlantic Treaty Organization AGARD: Neuilly-sur-Seine, France, 1993; ISBN: 92-835-0717-7.
13. Squire, L.C. Effects of Probe Supports on Measurements in Steam Turbines. In Proceedings of the Turbo Expo, Duesseldorf, Germany, 8–12 June 1986; ISBN: 978-0-7918-7928-3. [CrossRef]
14. Povey, T.; Jones, T.V.; Oldfield, M.L.G. On a Novel Annular Sector Cascade Technique. *J. Turbomach.* **2007**, *129*, 175–183. [CrossRef]
15. Landfester, C. Development of a High-Speed Annular Sector Cascade for Film Cooling Measurements in Nozzle Guide Vanes with Contoured Endwalls. Ph.D. Thesis, University of Kaiserslautern, Landau, Kaiserslautern, 2023;. [CrossRef]
16. Klappenberger, M.; Landfester, C.; Krewinkel, R.; Böhle, M. Influence of Radial Pressure Gradient on Secondary Flows: Numerical Study and Design Optimization for High-Speed Annular Sector Cascades, Paper No. ETC16-321, Hannover, Germany, 24–28 March 2025. Available online: https://www.euroturbo.eu/publications/conference-proceedings-repository/ (accessed on 20 April 2025).
17. Landfester, C.; Müller, G.; Krewinkel, R.; Domnick, C.; Böhle, M. Comparison of Film Cooling Performance for Different Purge Slot Configurations in a Cylindrical and State-of-the-Art Nozzle Guide Vane. *J. Turbomach.* **2022**, *144*, 031014. [CrossRef]
18. Menter, F.R. Two-equation eddy-viscosity turbulence models for engineering applications. *AIAA J.* **1994**, *32*, 1598–1605. [CrossRef]
19. Celik, I.B.; Ghia, U.; Roache, P.J.; Freitas, C.J.; Coleman, H.; Raad P.E. Procedure for Estimation and Reporting of Uncertainty Due to Discretization in CFD Applications. *J. Fluids Eng.* **2008**, *130*, 078001. [CrossRef]
20. Denton, J.D. The 1993 IGTI Scholar Lecture: Loss Mechanisms in Turbomachines. *J. Turbomach.* **1993**, *115*, 621–656. [CrossRef]
21. Moore, J.; Adhye, R.Y. Secondary Flows and Losses Downstream of a Turbine Cascade. *J. Eng. Gas Turbines Power* **1985**, *107*, 961–968. [CrossRef]
22. Landfester, C.; Krewinkel, R.; Domnick, C.; Böhle, M. A New High-Speed Annular Sector Test Rig for Film Cooling Performance Measurements, In Proceedings of the International Gas Turbine Congress, Kyoto, Japan, 26 November–1 December 2023.
23. Cumpsty, N.A.; Horlock, J.H. Averaging Nonuniform Flow for a Purpose. *J. Turbomach.* **2005**, *128*, 120–129. [CrossRef]